ARTICLES
https://doi.org/10.1038/s41928-018-0086-0
nature electronics

High-performance, multifunctional devices based on asymmetric van der Waals heterostructures

Ruiqing Cheng[1,2,3], Feng Wang[1,3], Lei Yin[1,2], Zhenxing Wang[1], Yao Wen[1,2], Tofik Ahmed Shifa[1,2] and Jun He[1,2]*

Two-dimensional materials are of interest for the development of electronic devices due to their useful properties and compatibility with silicon-based technology. Van der Waals heterostructures, in which two-dimensional materials are stacked on top of each other, allow different materials and properties to be combined and for multifunctional devices to be created. Here we show that an asymmetric van der Waals heterostructure device, which is composed of graphene, hexagonal boron nitride, molybdenum disulfide and molybdenum ditelluride, can function as a high-performance diode, transistor, photodetector and programmable rectifier. Due to the asymmetric structure of the device, charge-carrier injection can be switched between tunnelling and thermal activation under negative and positive bias conditions, respectively. As a result, the device exhibits a high current on/off ratio of 6×10^8 and a rectifying ratio of ~10^8. The device can also function as a programmable rectifier with stable retention and continuously tunable memory states, as well as a high program/erase current ratio of ~10^9 and a rectification ratio of ~10^7.

Two-dimensional (2D) materials, such as graphene and molybdenum disulfide, have various unique properties that could be used to build novel devices[1–8]. Due to weak van der Waals forces, different 2D materials can be vertically stacked to form artificial heterostructures—often referred to as van der Waals heterostructures (vdWHs)[9–11]—without being restricted by lattice mismatch. Based on mechanical exfoliation and manual stacking, various complex vdWHs, with atomically sharp interfaces, have been fabricated and used to create a range of devices, including atomically thin p–n junctions[12–14], tunnelling transistors[15,16], photodetectors[17–19], light-emitting diodes[20] and memory devices[21–23]. The heterostructures have also been used to build multifunctional devices[24–27]. For example, both high current rectification ratios (~4×10^5) and on/off ratios (~10^7) have been demonstrated with MoS_2–black phosphorus vertical heterostructures[25]. Alternatively, programmable p–n junctions have been created from vdWHs with a semifloating gate field-effect transistor (FET) configuration[26]. However, most of these functions were achieved in the conventional charge-carrier transport regime, which potentially limits device performance and integration.

Here, we report an asymmetric vdWH device that can function as a high-performance diode, transistor, photodetector and programmable rectifier. The heterostructure is composed of graphene, hexagonal boron nitride (h-BN), molybdenum disulfide (MoS_2) and molybdenum ditelluride ($MoTe_2$). The $MoTe_2$ is engineered as a physical and electronic buffer between the lateral MoS_2 channel and a metal electrode. Charge carriers can be injected into the channel by tunnelling or by thermal activation through the $MoTe_2/MoS_2$ p–n junctions under negative or positive bias. Consequently, our devices can be modulated and exhibit high current on/off and rectification ratios exceeding 10^8, which is one and two orders of magnitude higher, respectively, than previous reports[25]. Furthermore, the vdWH device also exhibits photodetection functionality and is capable of operating as a programmable rectifier with stable retention and multi-level storage. The corresponding program/erase current ratio and rectification ratio reach 10^9 and 10^7, respectively, which are one and three orders of magnitude higher than previously reported semifloating gate FETs[26]. (Supplementary Table 1 summarizes the figures of merit for different vdWH devices.)

Device structure and basic characterization

A schematic of our asymmetric heterostructure device is shown in Fig. 1a. It consists of a $MoTe_2$ flake sandwiched between the MoS_2 channel and a metal electrode. h-BN was used as the dielectric layer to facilitate scaling of the gate size and to reduce charge-carrier scattering. The electrode contacts for MoS_2 and $MoTe_2$ were made of chromium to reduce the Schottky barriers at the metal/semiconductor interfaces[14,28,29]. All of the devices were fabricated by mechanical exfoliation and a sacrificial layer-assisted manual-stacking method[30] (more details are provided in the Methods). The thicknesses of h-BN, MoS_2 and $MoTe_2$ flakes were defined to be ~13.8, 2.8 and 9.9 nm by atomic force microscopy (AFM), respectively.

The Raman spectra of MoS_2, $MoTe_2$ and their overlapped regions are shown in Fig. 1c. For the pristine MoS_2, two distinct peaks appear around 384.5 and 406.8 cm^{-1}, which are attributed to its E^1_{2g} and A_{1g} modes[31,32]. The position difference (22.3 cm^{-1}) between these two peaks indicates the existence of few-layer (3–4 layers) MoS_2, which agrees well with the results of AFM. The observed peaks of $MoTe_2$ at 172.7, 233.9 and 289.6 cm^{-1} correspond to its A_{1g}, E^1_{2g} and B^1_{2g} modes, revealing its multi-layer nature[28,33]. In the overlapped region, the intensities of the peaks are significantly reduced due to the strong interfacial coupling between two flakes, indicating the formation of a $MoS_2/MoTe_2$ heterostructure. The transfer characteristic of the multi-layer $MoTe_2$ is depicted in Supplementary Fig. 1. As expected, $MoTe_2$ exhibits a p-terminal dominated ambipolar conduction behaviour.

Figure 1d shows the current–voltage (I_{DS}–V_{DS}) output characteristics of the device under $V_G = 0$ at 300 K and 77 K. Note that the source electrode (the contact connected to MoS_2) is kept grounded in all of the measurements. Consistent with the asymmetric

[1]CAS Center for Excellence in Nanoscience, CAS Key Laboratory of Nanosystem and Hierarchical Fabrication, National Center for Nanoscience and Technology, Beijing, China. [2]University of Chinese Academy of Science, Beijing, China. [3]These authors contributed equally: Ruiqing Cheng, Feng Wang
*e-mail: hej@nanoctr.cn

© 2018 Macmillan Publishers Limited, part of Springer Nature. All rights reserved.

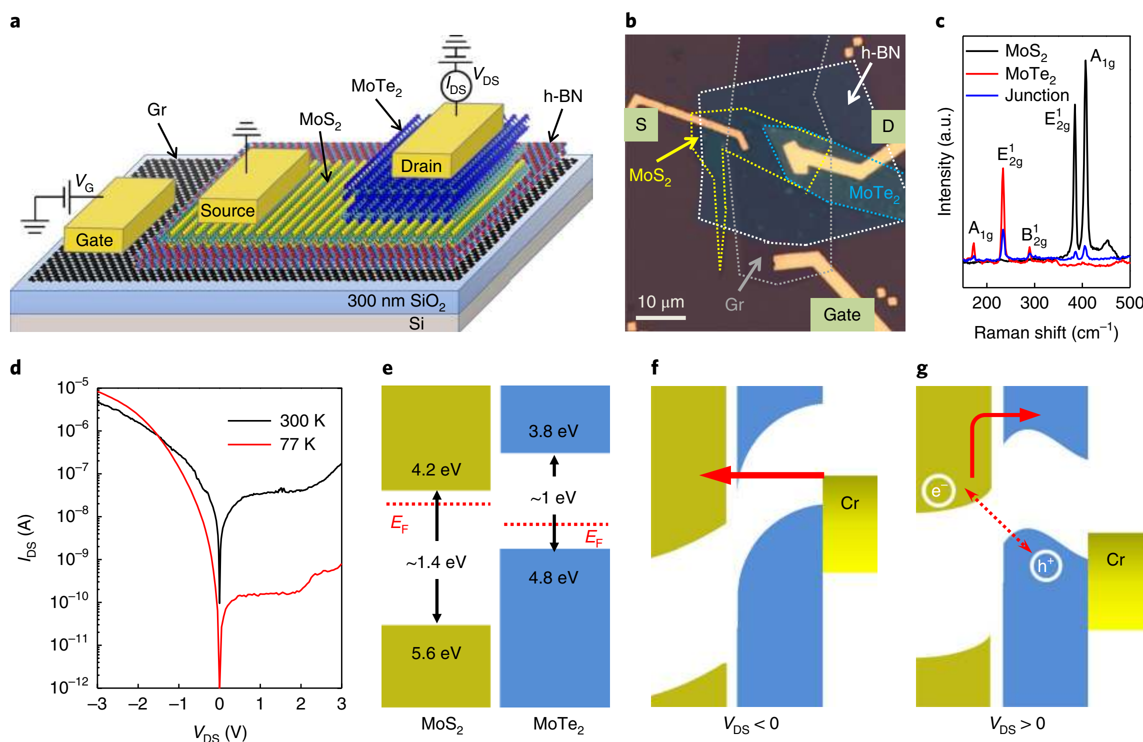

Fig. 1 | Device structure and basic characterization. a, Structure schematic of the device with a MoS_2/$MoTe_2$ junction as a channel at the top, h-BN as a dielectric layer in the middle, and graphene (Gr) as a gate electrode at the bottom. The source electrode (the contact connected to MoS_2) is grounded. **b**, Optical micrograph of the device. The boundaries of each flake are indicated by dotted lines with different colours. S, source; D, drain. **c**, Raman spectra of MoS_2, $MoTe_2$ and their overlapped regions on the h-BN substrate excited by 532 nm lasers. **d**, I_{DS}–V_{DS} curves of the MoS_2/$MoTe_2$ junction at two different temperatures of 300 and 77 K under $V_G = 0$, exhibiting different temperature dependence under the negative and positive bias conditions. **e–g**, Schematic band diagrams of the junction part in the isolated (**e**), negative bias (**f**) and positive bias (**g**) states. Forbidden bands, electrons and holes are represented by white regions, white circles with e⁻ and h⁺. Fermi level (E_F) positions, electron transport and electron–hole recombination are indicated by dashed lines, solid arrows and a dashed double-headed arrow, respectively.

structure, the device exhibits an asymmetrical electrical behaviour at 300 K, which becomes more striking at 77 K. Under positive bias, the current reduces significantly as the temperature decreases, whereas under negative bias, a different temperature dependence is observed in which the current increases under the high bias region. This behaviour can be attributed to the different operation modes of the device (see below).

The energy band diagrams of the heterostructure in the isolated and bias states are illustrated in Fig. 1e–g. Based on previous reports, the electron affinity and bandgap (E_g) of few-layer MoS_2 are around 4.2 and 1.4 eV, respectively[29,34,35]. For multi-layer $MoTe_2$, the corresponding values are 3.8 and 1 eV (refs [28,29]). Therefore, the heterostructure has a type-II band alignment. Under negative bias (Fig. 1f), the electrons/holes in MoS_2/$MoTe_2$ are depleted and the drain voltage will mainly drop across the junction part, giving rise to a strong electrical field. Hence, the energy bands of MoS_2 and $MoTe_2$ are bent severely. Combined with the ultrathin body thickness of $MoTe_2$, electron tunnelling can occur (especially under the high bias region), resulting in a large current value[36] (indicated by the red arrow in Fig. 1f). Here we do not display the interlayer recombination effect, considering the fact that electrons/holes in MoS_2/$MoTe_2$ are depleted under the large negative bias condition. In addition to the lack of temperature dependence, this tunnelling-dominated transport behaviour was further confirmed using the Fowler–Nordheim model (Supplementary Fig. 2)[30,37].

It is worth noting that over-barrier thermionic emission also contributes to the conduction process under the small bias region. However, when applying a positive bias (Fig. 1g), electrons (holes) are accumulated in MoS_2 ($MoTe_2$). As a result, the heterostructure reverts back to having a type-II band alignment and the $MoTe_2$ layer works as a semiconducting 'p-type vertical channel' in series with MoS_2, which can suppress the positive current and enhance the current asymmetry. Similar to the common p–n vertical junctions, the current is dominated by interlayer recombination of charge carriers (dashed double-headed arrow) and over-barrier free-electron transport (solid arrow), which are temperature dependent. This phenomenon is further confirmed by transport and photoresponse characterizations, which are discussed below. In short, under different bias conditions, the $MoTe_2$ flake serves as the 'tunnelling barrier' and 'vertical channel'.

Electrical transport properties

Figure 2a,b shows the I_{DS}–V_G transfer characteristics of the device under different fixed drain voltages at room temperature, and indicates a clear 'n-type' conducting behaviour. Due to the strain-free heterointerface and efficient control of gate electrostatics, the carrier density of MoS_2 and $MoTe_2$ can be modulated. Hence, our device exhibits electrically tunable electronic properties. The highest current on/off ratio of 6×10^8 is obtained under $V_{DS} = 2$ V. As discussed above, the device works as a type-II junction under a positive drain voltage, which is confirmed by its clear anti-ambipolar behaviour (grey area in Fig. 2a)[25,29,38,39]. The corresponding energy band diagrams are illustrated in Fig. 2e.

I_{DS}–V_G curves can be divided into three parts (Fig. 2a). In the first part (I), under positive gate voltage ($V_G > 0$), the Fermi levels of MoS_2 and $MoTe_2$ shift upwards, and the device operates as an n–n

© 2018 Macmillan Publishers Limited, part of Springer Nature. All rights reserved.

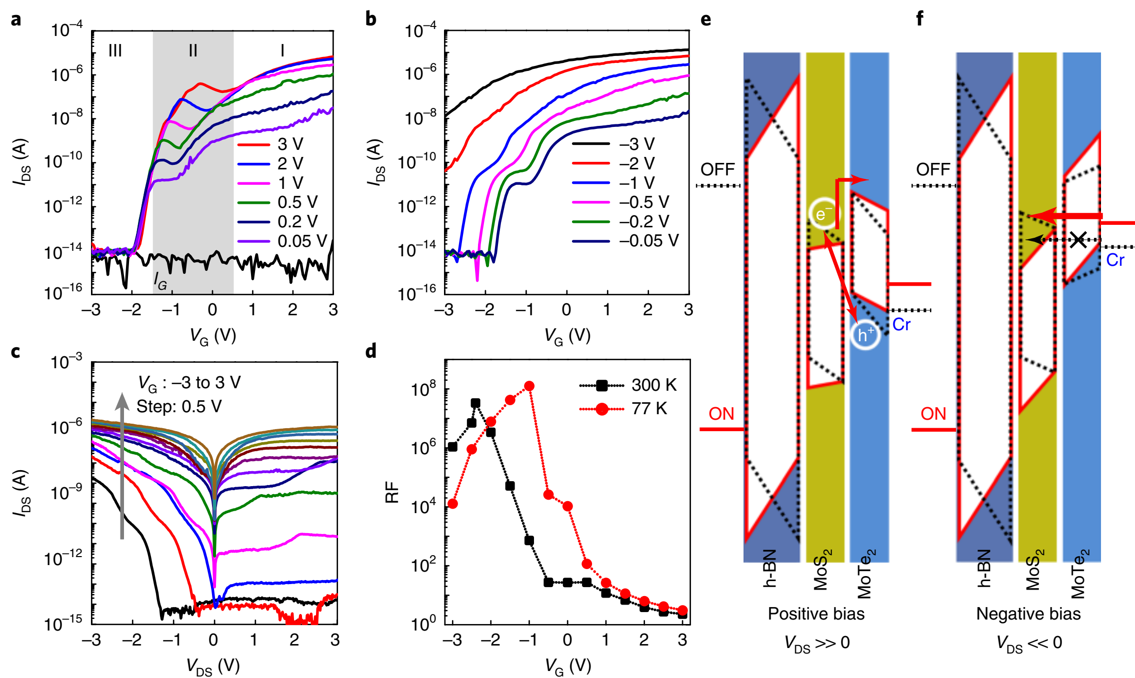

Fig. 2 | Electrical transport properties of the device. a,b, I_{DS}–V_G transfer curves under various drain voltages. The leakage current is shown by the black curve in **a**, and is in the range of tens of femtoamps. **c**, I_{DS}–V_{DS} output curves under various gate voltages from −3 to 3 V with a 0.5 V step. **d**, The plot of rectification ratio (RF = $I_{-3\,V}/I_{3\,V}$) versus gate voltage at 300 and 77 K. **e**,**f**, Schematic of the energy band diagrams in the positive bias (**e**) and negative bias (**f**) conditions under ON (red solid lines) and OFF (black dotted) states. Forbidden bands, electrons and holes are represented by white regions and white circles with e⁻ and h⁺. Electron transport and e–h recombination are indicated by one- and double-headed arrows, respectively.

junction. The drain current increases with the increasing gate voltage due to the higher electron concentration. The second part is the anti-ambipolar region (II): as the gate voltage decreases, the Fermi levels of MoS_2 and $MoTe_2$ shift down. As a result, $MoTe_2$ is tuned as p-type. However, MoS_2 remains n-type due to Fermi level pinning. Here, the device operates as a p–n junction, and the transport behaviour is dominated by the interlayer recombination between electrons in the conduction band of MoS_2 and holes in the valence band of $MoTe_2$. A peak exists where the densities of electrons and holes are comparable. The current values under $V_G = 0$ match well with those in the I_{DS}–V_{DS} curve (Fig. 1d), indicating the good repeatability. In the third part (III), the device turns off due to the depleted MoS_2 channel after applying a sufficiently high negative gate voltage. Under negative drain voltage, charge carriers can be injected into the channel by tunnelling under the negative scenario and the current is determined by the electrical field across the junction. The transfer curves in this case exhibit nearly monotonous variation (Fig. 2b), a characteristic that is more noticeable under high bias or low temperature conditions where the thermionic injection of the carriers is suppressed (Supplementary Fig. 6). The corresponding energy band diagrams are illustrated in Fig. 2f.

Under the same gate condition, a stronger electrical field will be generated by applying a larger bias (absolute value) because of the increasing potential difference between the drain and gate electrode. To switch off the device, a higher negative gate voltage is needed to fully modulate the band alignment of the $MoTe_2$/MoS_2 junction to a state where the tunnelling cannot happen: that is, inducing a negative V_{th} shift (Supplementary Fig. 4). Besides, under the negative bias conditions, no saturation current is observed over the test range (Supplementary Fig. 3). This high saturation voltage is also a typical feature of tunnelling. The dependency of transconductance on V_G was also investigated. Under the positively biased conditions, the device exhibits an obvious negative transconductance behaviour (more details are given in Supplementary Fig. 5).

To explore the current rectification and gate modulation ability of the device, we considered the different band alignments of the heterostructure under various external electrical field conditions. Figure 2c shows the I_{DS}–V_{DS} output curves under various gate voltages from −3 to 3 V with a 0.5 V step. The device exhibits a small (large) gate modulation under the negative (positive) bias, matching well with the transfer curves (Fig. 2a,b). Clear backward rectifying properties are observed. The current rectification ratios (RF = $I_{-3\,V}/I_{3\,V}$, versus V_G) at 300 and 77 K were extracted and are summarized in Fig. 2d. As the gate voltage increases, the rectification ratio first increases and then decreases. It is noteworthy that a rectification ratio as high as 3×10^7 is achieved under $V_G = -2.4$ V at 300 K (the corresponding I_{DS}–V_{DS} curve is displayed as the dark current in Fig. 3d). When the temperature reaches 77 K, the rectification ratio exceeds 10^8. To the best of our knowledge, these values are the highest reported to date for vdWHs.

Photoresponse properties

To further probe the different operation models of the device under various conditions, we conducted photoresponse measurements. Figure 3a shows the photocurrent (I_{ph}) map as a function of drain and gate voltages recorded under biasing conditions. Here, I_{ph} is defined as the difference between drain currents with and without a 473 nm laser ($I_{ph} = |I_{laser} - I_{dark}|$). Similar to the transfer curves under dark states (Fig. 2a,b), the photocurrent also exhibits distinctive behaviours under different bias conditions: that is, monotonous for negative or anti-ambipolar for positive. This difference becomes more pronounced between $V_{DS} = \pm 3$ V.

The corresponding I_{DS}–V_G curves under dark and illuminated states are shown in Fig. 3b. The drain current shows a significant increment under illumination for both the negative and positive

© 2018 Macmillan Publishers Limited, part of Springer Nature. All rights reserved.

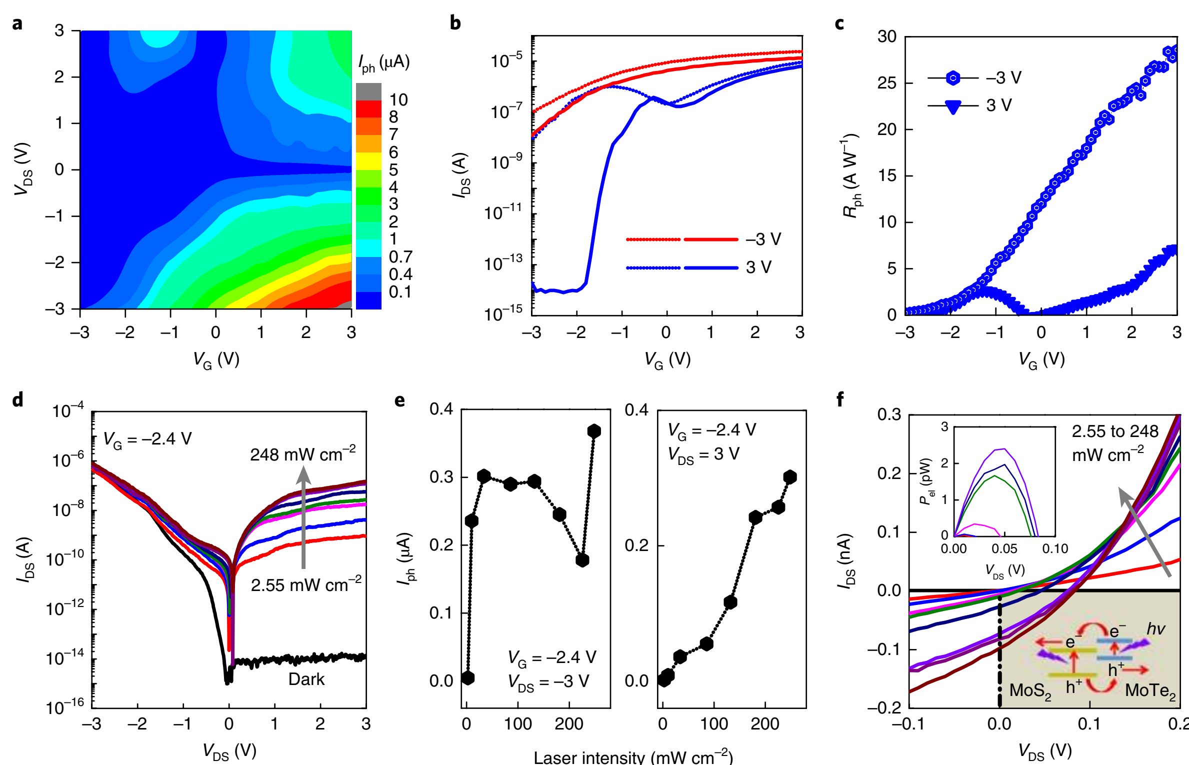

Fig. 3 | Photoresponse properties of the device. **a**, Photocurrent ($I_{ph} = |I_{laser} - I_{dark}|$) map with a fixed laser intensity ($P_{laser} = 248$ mW cm^{-2}) at various drain and gate voltages. **b**, I_{DS}–V_G curves of the device under dark (solid lines) and illuminated (dotted) states. V_{DS} was set as ±3 V. **c**, The corresponding photoresponsivity (R_{ph}) as a function of gate voltage. **d**, I_{DS}–V_{DS} curves of the device under a fixed $V_G = -2.4$ V in the dark and in the presence of a laser with different intensities from 2.55 to 248 mW cm^{-2}. **e**, Plot of the photocurrent along with laser intensities under a fixed $V_G = -2.4$ V and fixed $V_{DS} = \pm 3$ V. **f**, I_{DS}–V_{DS} curves at low bias were extracted from **d** to investigate its photovoltaic effect. Top inset, extracted electrical powers (defined as $P_{el} = I_{DS}V_{DS}$) versus V_{DS} under different laser intensities. Bottom inset, schematic band diagram of the junction at low positive bias under illumination.

bias conditions. Under negative bias ($V_{DS} = -3$ V), the charge carriers are injected into the channel by tunnelling and the device exhibits a unipolar behaviour similar to MoS_2 FETs, whereas under positive bias, a built-in electric field is introduced by the formation of p–n junctions. Hence, the photoresponse properties are dominated by the photovoltaic effect at small bias, which can be confirmed by its anti-ambipolar curve and the increased peak value under laser. At a large bias ($V_{DS} = 3$ V), the drift direction of photogenerated carriers is dominated by the external electric field and, thus, the drain current is the sum of dark current and photocurrent. However, when a small V_{DS} is applied, the drift of photogenerated carriers depends more on the built-in electric field at the MoS_2/$MoTe_2$ junction (the bottom inset of Fig. 3f), which can even induce a negative drain current. As shown in Supplementary Fig. 7, drain current (under illumination) at $V_{DS} = 0.05$ V shows a transition from positive to negative with the decreasing gate voltage.

To quantify the photoresponse performance, its photoresponsivity (R_{ph}) as a function of gate voltage was extracted (Fig. 3c). Photoresponsivity is defined as $R_{ph} = I_{ph}/(P_{laser}S)$ (refs [40,41]); here, P_{laser} is the laser intensity and S is defined as the total area of the overlapped junction and MoS_2 channel (~1.52×10^{-6} cm^2). When the V_G is set as 3 V, the largest responsivity reaches 28.6 and 7.2 A W^{-1} for $V_{DS} = -3$ and 3 V, respectively. The corresponding external quantum efficiency (EQE)[17], defined as $EQE = R_{ph}hc/q\lambda$, is calculated to be 7,522% and 1,882%. The high EQE is probably due to the photogating effect, which has been widely observed in 2D photodetectors and can be demonstrated by the shift of V_{th} while illuminated (Fig. 3b)[29].

Figure 3d shows the I_{DS}–V_{DS} curves under a fixed $V_G = -2.4$ V in the dark and in the presence of a laser with different intensities varied from 2.55 to 248 mW cm^{-2}. In this case, electrons are fully depleted in the MoS_2 channel and the heterostructure exhibits an ultralow dark current (~10^{-14} A) under positive bias. An obvious current increase was detected even for a laser intensity down to 2.55 mW cm^{-2}, indicating the sensitive photoresponse property of our device. When the laser intensity is set as 248 mW cm^{-2}, the drain current increases by seven orders of magnitude at $V_{DS} = 3$ V, matching the transfer curves well (Fig. 3b).

To quantitatively probe the laser intensity-controlled characteristic of our device, photocurrent values along with laser intensities under $V_{DS} = \pm 3$ V were extracted and plotted in Fig. 3e. As shown, the photocurrent exhibits irregular variations under negative bias with increasing laser intensities, whereas it increases linearly under positive bias. The tunnelling behaviour under negative bias can be confirmed by the Fowler–Nordheim model (Supplementary Fig. 7). For positive bias, the photocurrent approximately follows the power law $I_{ph} \sim P^{\beta}$ with $\beta = 1.09$, indicating a typical photogating effect, which is due to the depletion region (Supplementary Fig. 7).

The corresponding I_{DS}–V_{DS} curves at low bias are displayed in Fig. 3f to investigate its photovoltaic effect. Apparent open-circuit voltage (V_{OC}) and short-circuit current (I_{SC}) can be observed, and both increase with increasing laser intensities (Supplementary Fig. 8). Note that this photovoltaic effect occurs only when applying a negative gate voltage. These results further solidify the above discussed asymmetric charge injection mechanisms, and suggest that our asymmetric heterostructures could be of value in the development of optoelectronic and photovoltaic applications.

© 2018 Macmillan Publishers Limited, part of Springer Nature. All rights reserved.

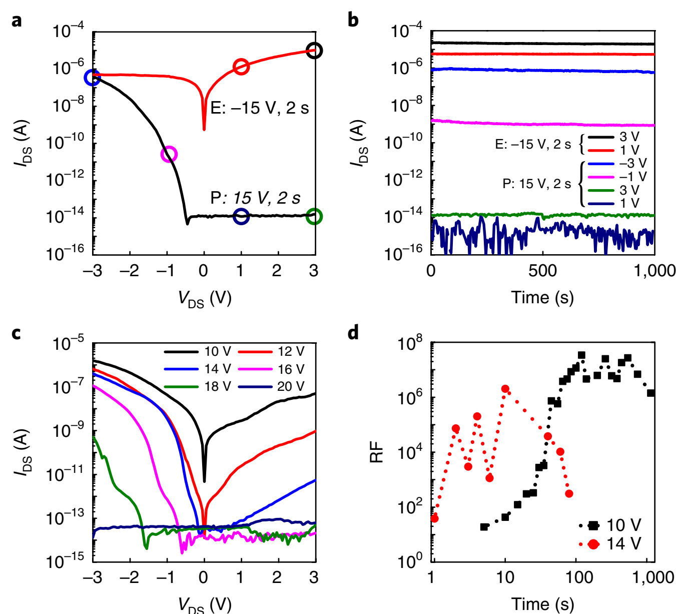

Fig. 4 | High-performance programmable rectifier. a, The program (P, black curve) and erase (E, red) states of the device after applying a ± 15 V back-gate pulse with 2 s duration. **b**, Retention performance of the program and erase states with different reading voltages. **c**, I_{DS}–V_{DS} curves of the device after applying different program voltages with 2 s duration. **d**, The plot of rectification ratio along with the program time by applying two different program voltages of 10 and 14 V.

High-performance programmable rectifier

Memory devices are important electronic components of digital circuits. By taking advantage of graphene's capability to store charges, we show that our vertically stacked vdWHs can operate as non-volatile memory, in which MoS_2/$MoTe_2$, h-BN and graphene are treated as a channel, a tunnelling layer and a floating gate, respectively. The device can operate in different memory states by tuning the back-gate voltage. The floating gate exhibits a positive (negative) gate-like behaviour after a negative (positive) back-gate pulse is applied[21,22,42]. The relevant band diagrams to interpret this behaviour are presented in Supplementary Fig. 9. In particular, with a positive back-gate pulse, electrons in the channel will be transferred into and accumulated in the graphene layer, corresponding to the program state (P). The stored electrons can play a role like a negative gate voltage. Therefore, the phenomenon observed under negative gate voltage can be maintained in this state.

Considering the excellent current rectification characteristics of our device structure, a high-performance programmable rectifier is expected. For example, after applying a +15 V back-gate pulse with 2 s duration, the device exhibits an ultrahigh rectification ratio exceeding 2×10^7 (displayed as the black curve in Fig. 4a). Conversely, with a negative back-gate pulse, electrons in the graphene layer will tunnel into the channel, resulting in an erase state. Good retention performance of these two states is also demonstrated. As shown in Fig. 4b, the program state with different reading voltages of ±1, ±3 V and the erase state with 1, 3 V all showed no appreciable change, after removing the corresponding back-gate pulses within experimental timescales (~1,000 s). When the reading voltage was set as 3 V, a high program/erase current ratio of 10^9 was obtained, which makes it easy to read out the memory state. It is worth noting that when the reading voltage reduces to 1 V, the device still exhibits an ultrahigh current program/erase ratio of around 10^9 and a rectification ratio over 10^5. The low current (~10^{-14} A) under the program state suggests that the approach has significant potential in the development of low-power devices.

The tunable memory state of a given device is crucial to realize multi-bit data storage and large memory density. It is known that the Fermi level of graphene can be easily tuned due to its low density of states[15]. Therefore, the memory state is sensitive to the number of stored electrons in the graphene layer, which were determined by program voltage and time. Generally, with a larger back-gate pulse or longer program time, more electrons will tunnel into and be stored in the graphene layer.

Figure 4c shows the I_{DS}–V_{DS} curves of the device after applying different back-gate pulses with 2 s duration. The current under both positive and negative bias conditions decreased with the increasing pulse values, although the positive current decreased faster. This phenomenon is in accordance with Fig. 2c: that is, more stored electrons equivalent to more negative gate voltage. The corresponding current rectification ratios were extracted and are shown in Supplementary Fig. 10. As the program voltage increases, firstly a rise is observed, which is then followed by a decrease.

The relationship between memory states and program time was also studied. Figure 4d illustrates the influence of program time on the rectification ratio. When a +14 V back-gate pulse is applied, the rectification ratio increases firstly and then decreases with the increasing duration time. However, with a +10 V pulse, the rectification ratio shows a saturating dependence as a function of the program time after its initial rise due to the small potential difference between the gate and the channel. The corresponding I_{DS}–V_{DS} curves are presented in Supplementary Fig. 10. Hence, by applying different program voltages and time, we can get different memory states. In short, due to the high performance of the asymmetric vdWHs, our 2D programmable rectifier shows stable retention, continuously tunable memory states, low power consumption, and a high program/erase current ratio and rectification ratio.

Conclusions

We have shown that asymmetric heterostructures composed of graphene, h-BN, MoS_2 and $MoTe_2$ can be used to create high-performance multifunctional devices. With our approach, current modulation with a high current on/off ratio of 6×10^8 and a rectification ratio of 10^8, as well as notable photodetection capabilities, can be achieved with the same device. We have also evaluated the performance of our vdWH device as a programmable rectifier, which exhibits stable retention, multi-level storage, a significant program/erase current ratio (~10^9) and a high rectification ratio (2×10^7). This combination of high performance and multifunction suggests, we believe, that our approach could provide a valuable direction for creating future electronics and optoelectronic devices based on the integration of 2D materials.

Methods

Device fabrication. Heterostructure preparation began with exfoliation on 300 nm SiO_2/Si substrates of bulk graphite crystals (99.995%, HQ Graphene). Then, h-BN, MoS_2 and $MoTe_2$ layers (all purchased from SPI) were mechanically exfoliated onto the PPC/SiO_2/Si substrates and sequentially transferred onto the bottom graphene layer. Finally, electrodes were fabricated by standard electron-beam lithography and metal deposition of Cr/Au (10/60 nm). Most processes except the short time of transfer process were conducted in a nitrogen-protected environment with O_2 and H_2O concentration <1 ppm.

Characterization. The thickness and material quality of flakes were characterized by optical microscopy (Olympus BX51M), Raman microscopy (Renishaw InVia, 532 nm excitation laser) and AFM (Bruker Icon), respectively. Electrical properties were characterized by a probe station (Lakeshore, TTP4) equipped with a Keithley 4200 semiconductor analyser. The photoresponse properties were measured using a 473 nm laser with a diameter of 5 mm and maximum laser intensity of 12.77 mW (RGBLase). The laser intensity was varied using a continuous laser attenuator. All of the electrical measurements were performed under high vacuum (~10^{-6} torr) to eliminate the possible influence of the atmosphere.

© 2018 Macmillan Publishers Limited, part of Springer Nature. All rights reserved.

Data availability. The data that support the plots within this paper and other findings of this study are available from the corresponding author upon reasonable request.

Received: 8 February 2018; Accepted: 15 May 2018;
Published online: 13 June 2018

References

1. Novoselov, K. S. et al. Electric field effect in atomically thin carbon films. *Science* **306**, 666–669 (2004).
2. Radisavljevic, B., Radenovic, A., Brivio, J., Giacometti, V. & Kis, A. Single-layer MoS_2 transistors. *Nat. Nanotech.* **6**, 147–150 (2011).
3. Desai, S. B. et al. MoS_2 transistors with 1-nanometer gate lengths. *Science* **354**, 99–102 (2016).
4. Xu, K. et al. Sub-10 nm nanopattern architecture for 2D material field-effect transistors. *Nano Lett.* **17**, 1065–1070 (2017).
5. Lopez-Sanchez, O., Lembke, D., Kayci, M., Radenovic, A. & Kis, A. Ultrasensitive photodetectors based on monolayer MoS_2. *Nat. Nanotech.* **8**, 497–501 (2013).
6. Mak, K. F., McGill, K. L., Park, J. & McEuen, P. L. The valley Hall effect in MoS_2 transistors. *Science* **344**, 1489–1492 (2014).
7. Bie, Y.-Q. et al. A $MoTe_2$-based light-emitting diode and photodetector for silicon photonic integrated circuits. *Nat. Nanotech.* **12**, 1124–1129 (2017).
8. Wang, Q. H., Kalantar-Zadeh, K., Kis, A., Coleman, J. N. & Strano, M. S. Electronics and optoelectronics of two-dimensional transition metal dichalcogenides. *Nat. Nanotech.* **7**, 699–712 (2012).
9. Geim, A. K. & Grigorieva, I. V. Van der Waals heterostructures. *Nature* **499**, 419–425 (2013).
10. Novoselov, K. S., Mishchenko, A., Carvalho, A. & Castro Neto, A. H. 2D materials and van der Waals heterostructures. *Science* **353**, aac9439 (2016).
11. Liu, Y. et al. Van der Waals heterostructures and devices. *Nat. Rev. Mater.* **1**, 16042 (2016).
12. Lee, C. H. et al. Atomically thin p–n junctions with van der Waals heterointerfaces. *Nat. Nanotech.* **9**, 676–681 (2014).
13. Furchi, M. M., Pospischil, A., Libisch, F., Burgdorfer, J. & Mueller, T. Photovoltaic effect in an electrically tunable van der Waals heterojunction. *Nano Lett.* **14**, 4785–4791 (2014).
14. Wang, F. et al. Tunable GaTe–MoS_2 van der Waals p–n junctions with novel optoelectronic performance. *Nano Lett.* **15**, 7558–7566 (2015).
15. Britnell, L. et al. Field-effect tunneling transistor based on vertical graphene heterostructures. *Science* **335**, 947–950 (2012).
16. Roy, T. et al. Dual-gated MoS_2/WSe_2 van der Waals tunnel diodes and transistors. *ACS Nano* **9**, 2071–2079 (2015).
17. Britnell, L. et al. Strong light–matter interactions in heterostructures of atomically thin films. *Science* **340**, 1311–1314 (2013).
18. Yu, W. J. et al. Highly efficient gate-tunable photocurrent generation in vertical heterostructures of layered materials. *Nat. Nanotech.* **8**, 952–958 (2013).
19. Zhou, X. et al. Tunneling diode based on WSe_2/SnS_2 heterostructure incorporating high detectivity and responsivity. *Adv. Mater.* **30**, 1703286 (2018).
20. Withers, F. et al. Light-emitting diodes by band-structure engineering in van der Waals heterostructures. *Nat. Mater.* **14**, 301–306 (2015).
21. Bertolazzi, S., Krasnozhon, D. & Kis, A. Nonvolatile memory cells based on MoS_2/graphene heterostructures. *ACS Nano* **7**, 3246–3252 (2013).
22. Choi, M. S. et al. Controlled charge trapping by molybdenum disulphide and graphene in ultrathin heterostructured memory devices. *Nat. Commun.* **4**, 1624 (2013).
23. Vu, Q. A. et al. Two-terminal floating-gate memory with van der Waals heterostructures for ultrahigh on/off ratio. *Nat. Commun.* **7**, 12725 (2016).
24. Yu, W. J. et al. Vertically stacked multi-heterostructures of layered materials for logic transistors and complementary inverters. *Nat. Mater.* **12**, 246–252 (2013).
25. Huang, M. et al. Multifunctional high-performance van der Waals heterostructures. *Nat. Nanotech.* **12**, 1148–1154 (2017).
26. Li, D. et al. Two-dimensional non-volatile programmable p–n junctions. *Nat. Nanotech.* **12**, 901–906 (2017).
27. Heo, J. et al. Reconfigurable van der Waals heterostructured devices with metal–insulator transition. *Nano Lett.* **16**, 6746–6754 (2016).
28. Yin, L. et al. Ultrahigh sensitive $MoTe_2$ phototransistors driven by carrier tunneling. *Appl. Phys. Lett.* **108**, 043503 (2016).
29. Wang, F. et al. Configuration-dependent electrically tunable van der Waals heterostructures based on $MoTe_2$/MoS_2. *Adv. Funct. Mater.* **26**, 5499–5506 (2016).
30. Cheng, R. et al. Multifunctional tunneling devices based on graphene/*h*-BN/$MoSe_2$ van der Waals heterostructures. *Appl. Phys. Lett.* **110**, 173507 (2017).
31. Liu, K.-K. et al. Growth of large-area and highly crystalline MoS_2 thin layers on insulating substrates. *Nano Lett.* **12**, 1538–1544 (2012).
32. Lee, Y. H. et al. Synthesis of large-area MoS_2 atomic layers with chemical vapor deposition. *Adv. Mater.* **24**, 2320–2325 (2012).
33. Wang, Z. et al. Electrostatically tunable lateral $MoTe_2$ p–n junction for use in high-performance optoelectronics. *Nanoscale* **8**, 13245–13250 (2016).
34. Padilha, J. E., Peelaers, H., Janotti, A. & Van de Walle, C. G. Nature and evolution of the band-edge states in MoS_2: From monolayer to bulk. *Phys. Rev. B* **90**, 205420 (2014).
35. Mak, K. F., Lee, C., Hone, J., Shan, J. & Heinz, T. F. Atomically thin MoS_2: a new direct-gap semiconductor. *Phys. Rev. Lett.* **105**, 136805 (2010).
36. Georgiou, T. et al. Vertical field-effect transistor based on graphene–WS_2 heterostructures for flexible and transparent electronics. *Nat. Nanotech.* **8**, 100–103 (2013).
37. Ma, Q. et al. Tuning ultrafast electron thermalization pathways in a van der Waals heterostructure. *Nat. Phys.* **12**, 455–459 (2016).
38. Nourbakhsh, A., Zubair, A., Dresselhaus, M. S. & Palacios, T. Transport properties of a MoS_2/WSe_2 heterojunction transistor and its potential for application. *Nano Lett.* **16**, 1359–1366 (2016).
39. Wang, Z., He, X., Zhang, X. X. & Alshareef, H. N. Hybrid van der Waals p–n heterojunctions based on SnO and 2D MoS_2. *Adv. Mater.* **28**, 9133–9141 (2016).
40. Konstantatos, G. & Sargent, E. H. Nanostructured materials for photon detection. *Nat. Nanotech.* **5**, 391–400 (2010).
41. Cheng, R. et al. Ultrathin single-crystalline CdTe nanosheets realized via van der Waals epitaxy. *Adv. Mater.* **29**, 1703122 (2017).
42. Li, D., Chen, M., Zong, Q. & Zhang, Z. Floating-gate manipulated graphene–black phosphorus heterojunction for nonvolatile ambipolar Schottky junction memories, memory inverter circuits, and logic rectifiers. *Nano Lett.* **17**, 6353–6359 (2017).

Acknowledgements

This work was supported by the Ministry of Science and Technology of China (no. 2016YFA0200700), the National Natural Science Foundation of China (nos. 61625401, 61474033, 61574050 and 11674072), the Strategic Priority Research Program of the Chinese Academy of Sciences (grant no. XDA09040201) and the CAS Key Laboratory of Nanosystem and Hierarchical Fabrication. The authors also gratefully acknowledge the support of the Youth Innovation Promotion Association CAS.

Author contributions

J.H. conceived and supervised the project. R.C. fabricated the devices and performed electrical and optoelectronic measurements. L.Y. carried out the Raman and AFM measurements. R.C., F.W. and J.H. analysed the data and co-wrote the manuscript in consultation with L.Y., Z.W., Y.W. and T.A.S.

Competing interests

The authors declare no competing interests.

Additional information

Supplementary information is available for this paper at https://doi.org/10.1038/s41928-018-0086-0.

Reprints and permissions information is available at www.nature.com/reprints.

Correspondence and requests for materials should be addressed to J.H.

Publisher's note: Springer Nature remains neutral with regard to jurisdictional claims in published maps and institutional affiliations.

© 2018 Macmillan Publishers Limited, part of Springer Nature. All rights reserved.